

# Non-Uniform Deblurring in HDR Image Reconstruction

C. S. Vijay, C. Paramanand, A. N. Rajagopalan, *Senior Member, IEEE*,  
and Rama Chellappa, *Fellow, IEEE*

**Abstract**—Hand-held cameras inevitably result in blurred images caused by camera-shake, and even more so in high dynamic range imaging applications where multiple images are captured over a wide range of exposure settings. The degree of blurring depends on many factors such as exposure time, stability of the platform, and user experience. Camera shake involves not only translations but also rotations resulting in nonuniform blurring. In this paper, we develop a method that takes input non-uniformly blurred and differently exposed images to extract the deblurred, latent irradiance image. We use transformation spread function (TSF) to effectively model the blur caused by camera motion. We first estimate the TSFs of the blurred images from locally derived point spread functions by exploiting their linear relationship. The scene irradiance is then estimated by minimizing a suitably derived cost functional. Two important cases are investigated wherein 1) only the higher exposures are blurred and 2) all the captured frames are blurred.

**Index Terms**—Computational photography, motion blur, high dynamic range imaging, image deblurring.

## I. INTRODUCTION

HIGH dynamic range (HDR) imaging is concerned with extraction of latent scene irradiance. The variation in the magnitude of the irradiance can be as wide as 14 orders in the log unit scale. The CCD/CMOS sensors are either not sensitive enough to collect the reflected energy (dark scenes) or do not have the capacity to collect all the energy incident and represent it as a unique value (scenes with light sources). Hence, scenes with a large dynamic range either appear dark or saturated. HDR cameras are commercially available but these are very expensive. Over the years, several algorithmic approaches for estimation of scene irradiance [6], [22], [24] have been suggested. The basic idea is to capture multiple images of a scene with different exposure settings and algorithmically extract HDR information from these observations. For

Manuscript received August 26, 2012; revised February 19, 2013; accepted March 19, 2013. Date of publication April 12, 2013; date of current version August 28, 2013. The associate editor coordinating the review of this manuscript and approving it for publication was Prof. Vishal Monga.

C. S. Vijay, C. Paramanand, and A. N. Rajagopalan are with the Department of Electrical Engineering, Indian Institute of Technology, Chennai 600 036, India (e-mail: csv2000@gmail.com; paramanand@gmail.com; raju@ee.iitm.ac.in).

R. Chellappa is with the Center for Automation Research, Department of Electrical and Electronic Engineering, University of Maryland, College Park, MD 20742-3275 USA (e-mail: rama@umiacs.umd.edu).

This paper has supplementary downloadable material available at <http://ieeexplore.ieee.org>, provided by the author. The material includes illustration of a technique that is described in the paper in the form of a pdf document. The size of the document is 2.3 MB.

Color versions of one or more of the figures in this paper are available online at <http://ieeexplore.ieee.org>.

Digital Object Identifier 10.1109/TIP.2013.2257809

a real world scene, the exposure times can vary from values as small as  $\frac{1}{500}$ s to as high as 5s. An important and practical issue associated with long exposure times is that of image blurring. With recent advancements, consumer cameras have become small, light-weight and high-resolution, and offer options for even varying the lens parameters. However, these cameras are inherently difficult to hold steady and any incidental shake of the camera will result in blurring. Motion blur can be avoided provided the camera is placed on a firm support. However, carrying such sturdy accessories can be cumbersome. Interestingly, there is strong evidence that most consumer photographs are taken with handheld cameras [10]. Even if one were to use light weight tripods and monopods, blur cannot be completely avoided [7]. Thus, it is not surprising that motion deblurring has attracted considerable attention. In the scenario of HDR imaging, the need for longer exposure times increases the possibility of degradation due to motion blur [21]. Furthermore, in places such as heritage sites or museums, there are restrictions on carrying tripods [1]. Hence, in HDR imaging, developing algorithms to remove motion blur becomes all the more important.

A set of non-uniformly blurred images captured with a Canon 60D is shown in Figure 1(a). The problem of scene irradiance reconstruction in the presence of blurred observations was first discussed by Lu et al. [21]. They consider a set of differently exposed but *uniformly* blurred images. The convolution blur model used in [21] restricts camera motion to in-plane translation. A possible solution is to restore non-uniformly blurred images using a technique such as [34] and find the HDR image using the deblurred set. But such a naive approach is subject to accuracy of deblurring and can contain artifacts. Here, we discuss a method for simultaneous deblurring and HDR imaging of a scene using a set of differently exposed and *non-uniformly* blurred images

## A. Related Works

The focus of initial works has been on determining the camera response function (CRF). In their leading work, Mann and Picard [22] determined the response at a sequence of points by assuming a parameterized model for the CRF in the form of a gamma curve.Debevec and Malik [6] determine the log of the inverse camera response without using a parametric form. Mitsunaga and Nayar [24] assumed that the exposure ratios are initially unknown and that the inverse response function can be closely approximated by a polynomial. They then iteratively estimate the response and the ratios. All of the above methods assume that the frames are registered and



Fig. 1. (a) Three blurred observations captured at exposure times of  $\frac{1}{6}$ ,  $\frac{1}{2}$  and 2s, respectively. (b) The resulting tone-mapped HDR image obtained using our method.

the scene is static. Once the CRF is estimated, the weighted average of the irradiance images for different exposures is obtained. The exposure of the camera can also be varied by changing the area (diameter) of the aperture. Hasinoff and Kutulakos [16] use differently exposed images captured by varying the aperture size to estimate the latent scene irradiance image. The irradiance image is tone-mapped to low dynamic range (LDR) image that can be displayed with only 8 bits/channel using HDR compression algorithms such as those given in [2], [8], [9], [27].

In fusion-based approaches in [23], [25], [26], [33], the weights of the exposures are determined using features derived from the images. The approach is easy and fast to implement and the output is an HDR-equivalent LDR image. Mertens et al. [23] weigh the exposures based on local contrast, saturation and well-exposedness of a pixel. Ward [33] chooses the weights based on the median threshold bitmap (MTB) of each of the exposures. Fattal et al. [9] and Raskar et al. [26] propose fusion based on the gradient images of the different frames. Except for [33], all the other works assume that the frames in the dataset are registered and the scene is static.

The restoration of motion blurred images is an established area of research. Several approaches exist that solve for the image and the blur kernel (blind deconvolution) [3], [10], [18]. Fergus et al. [10] have proposed a blind deconvolution algorithm using natural image statistics as prior. In [28], a method is proposed to enhance deconvolution results by using improved noise models to suppress artifacts. In [3], the sparse nature of the motion blur kernel is exploited to give a framelet-based solution. The motion deblurring problem being highly ill-posed has even attracted several multi-channel approaches. Sroubek and Flusser [30] proposed a multi-channel alternating minimization algorithm based on total variation and Mumford-Shah functional. Yuan et al. [37] describe image restoration using blurry/noisy image pairs. In a very recent work, the effect of CRF's nonlinearity on deblurring has been discussed [17]. The space-invariant blur considered in these works can be modeled using a convolution model. However, as shown in [18], [34] blurring due to camera shake is typically space-variant. In fact, rotation has greater influence on blurring than translation.

The problem of handling non-uniform motion blur is discussed in [15], [29], [31], [34]. Tai et al. [31] describe the blurring process using a projective motion model and accordingly modify the Richardson-Lucy algorithm succinctly to estimate the original image. Gupta et al. [15] have suggested that the camera motion can be modeled as a motion density function and the blur at each pixel can be obtained using this function.

Whyte et al. [34] use a space-variant blur kernel derived from 3 degrees of rotation and incorporate them into the deblurring technique of Fergus et al. [10]. The blur models considered in [15], [31], [34] regard the image formation process as an integral sum of photographs of the scene captured at shifted positions. Also, all the above non-uniform deblurring works ignore the effects of parallax. For translational camera motion, Sorel and Flusser [29] proposed a variational approach to restore space-variantly blurred images. A very recent work by Chandramouli and Rajagopalan [4] estimates depth of a 3D scene using parallax induced motion blur as a cue while considering camera in-plane rotations.

Notably, none of the non-uniform deblurring algorithms take into account the high dynamic nature of real scenes. As discussed earlier, Lu et al. [21] address the problem of obtaining the HDR image from a set of *uniformly* blurred (and possibly shifted) images. The uniformly blurred images are first aligned using MTB [33]. Then, they iteratively estimate the blur kernels, the HDR image and the CRF. Although this is encouraging, the space-invariant formulation falls short of representing a more realistic scenario where camera rotation effects are also present. Zhang et al. [38] consider HDR imaging while compensating for camera motion, but restrict the application to high-end cameras having more quantization levels. They obtain the latent scene image by denoising a sequence of non-blurred images captured at high ISO and low exposure settings. However, they do not include the possibility of non-uniform blurring due to camera rotation. Also their assumption that capturing images at high ISO settings can cover the entire dynamic range may not be justified for all real world scenes.

In this paper, our objective is to obtain the latent scene irradiance from a set of *non-uniformly* blurred images captured using a hand-held camera. In our approach, we use the notion of transformation spread function (TSF) which expresses a non-uniformly blurred image as a weighted sum of different transformations of the latent image [4]. We first estimate the TSFs of the blurred images using locally estimated point spread functions (PSFs). We follow this approach because it is accurate and estimating TSF from PSFs is simpler than directly estimating TSF. Moreover, techniques already exist for PSF estimation [30] which is an extensively researched topic. We then estimate the latent irradiance image by iteratively minimizing the cost function based on the relationship that exists among the TSF, latent scene irradiance and the blurred irradiance image. Because the different intensity images are not directly comparable in the intensity domain, the above procedure is executed in the irradiance domain. For the example of Figure 1, we have shown the

output of our method in Figure 1(b). Note that our result is not only uniformly illuminated but is also deblurred everywhere.

While capturing multiple images with a hand-held camera, occasionally there can be a shift in the camera center. Although a local PSF will reflect this shift, it will usually require very large PSFs to do so and this can complicate the already ill-posed estimation process. Registering the images will help in reducing the sizes of blur kernels. Lu *et. al.* [21] use MTB [33] for registration but it is too laborious for our purpose. We use scale invariant feature transform (SIFT) feature-based registration which although not very precise for blurred images, is sufficient for the problem on hand.

In a preliminary version of this work [32], we had considered the input data to consist of both non-blurred and blurred observations, assuming that the effect of camera-shake is significant only beyond a certain exposure duration. The work described here extends the work in [32] in many ways. Here, we also address the important situation where all the input observations are blurred. In [32], the local PSFs were estimated with respect to a non-blurred lower exposure. Here, we extend PSF estimation for the case of all-blurred data. Since the estimation process is blind it is accurate upto in-plane translations. We also propose a method to compensate for the unknown shifts in the PSFs and TSF using intra and inter-frame alignment. We also show how to handle the case of large mis-alignments across frames. Finally, the level of explanation given in this paper is quite exhaustive in comparison to [32].

We list below the main contributions of our work:

- This is the first attempt of its kind to obtain HDR scene irradiance from a set of *non-uniformly* blurred images. Our effort leads to an elegant generalization of the current state-of-the-art system proposed by Lu *et al.* [21].
- We propose different ways of handling i) non-blurred/blurred observations, and ii) the situation of all-blurred observations along with associated alignment issues.
- Although the TSF model has been previously used on intensity images, this is the first work to effectively employ this model in the irradiance domain.

The rest of the paper is organized as follows: In section II, we describe the TSF model and elaborate upon its estimation process. The task of irradiance estimation is discussed in section III where we discuss the formulation for simultaneous deblurring and recovery of the latent HDR irradiance image under two different scenarios, namely, non-blurred/blurred and all-blurred observations. In section IV, we substantiate the proposed scheme with experimental examples. We conclude with section V.

## II. IMAGE FORMATION MODEL

### A. Image Accumulation

In a typical off-the-shelf camera pipeline [6], the scene radiance gets attenuated and integrated due to the lens and the aperture of the camera to yield the irradiance of the scene.

The pixel intensity value in an image is a monotonic but nonlinear function of the irradiance and exposure period. The light energy accumulated is given by

$$X = \int_{t=0}^{\Delta t} E dt + n \quad (1)$$

where  $E$  is the irradiance,  $\Delta t$  is the exposure time, and  $n$  is additive noise. A series of specialized algorithms alter the collected data in real-time to map the irradiance values to the final image intensities. Cameras implement the image-pipeline in hardware. Typical steps include image sensor corrections, digitization, noise reduction, gamma correction, color-space conversion, chroma subsampling, compression and storage/transmission. The net effect of the above steps with respect to exposure time is a nonlinear mapping between the scene irradiance and the image intensity referred to as the CRF [13], [14]. The CCD/CMOS camera sensors display this nonlinear response with an upper saturation level above which different exposures are indistinguishable. Standard HDR techniques such as [6], [24] describe methods for the estimation of CRF. The relation between irradiance and final intensity may be written as  $Z = f(E\Delta t)$ . Given the intensity image and CRF, an estimate of the irradiance can be obtained as  $B = f^{-1}(Z)/\Delta t$  where  $f^{-1}$  is the inverse of the smooth and monotonous CRF. Note that due to the saturation effects (at higher values) and sensor insensitivity (at lower values),  $B$  is never the same as the original irradiance  $E$ .

From a geometrical perspective, the 2D irradiance image is the projection of the 3D scene, which is mapped to intensity values. For a static scene with constant depth, the 2D irradiance images projected at different instances of time can be related using a homography. The transformation  $\Gamma$  can be written as

$$\Gamma = K_v \left( R + \frac{1}{d_o} T [0 \ 0 \ 1] \right) K_v^{-1} \quad (2)$$

where  $K_v$  is  $3 \times 3$  camera matrix,  $R$  is the rotation matrix, and  $T$  is  $3 \times 1$  translation vector  $[T_X \ T_Y \ T_Z]^T$ . The matrix  $K_v$  is assumed to be of the form

$$K_v = \begin{bmatrix} v & 0 & 0 \\ 0 & v & 0 \\ 0 & 0 & 1 \end{bmatrix} \text{ and } R = e^\Phi$$

where

$$\Phi = \begin{bmatrix} 0 & -\theta_z & \theta_y \\ \theta_z & 0 & -\theta_x \\ -\theta_y & \theta_x & 0 \end{bmatrix}$$

Here,  $\theta_x$ ,  $\theta_y$  and  $\theta_z$  represent rotations about the three axes. The total energy accumulated is a sum of projectively warped latent irradiance images. If  $\Gamma_t$  refers to the transformation at instant  $t$  of the latent irradiance image  $E$ , then the accumulated result over the exposure duration  $\Delta t$  is given by

$$Z = f \left( \int_{t=0}^{\Delta t} \Gamma_t (E) dt \right) \quad (3)$$

where  $Z$  is the final intensity image. The various transformations  $\Gamma_t$  indicate the location of the camera at time  $t$ , i.e., they indicate the path of the camera motion. When averaging

over time, the temporal information is lost. In our work, we adopt the transformation spread function (TSF) model which averages these images over transformations to describe the blurred image.

### B. TSF and its Estimation

The notion of TSF or set of homographies for modeling motion blur has been recently discussed in [4], [15], [34]. For a scene with minimal depth variations, the image resulting from camera shake can be described as a weighted sum of the homographies of the latent scene image. A camera has 6 degrees of freedom viz. 3 translations ( $t_x, t_y$  and  $t_z$ ) and 3 rotations (yaw  $\theta_y$ , pitch  $\theta_x$ , and roll  $\theta_z$ ). However, when the scene is largely flat (as assumed in this work), the blur induced by out-of-plane rotation is similar to that of translation. Also, while capturing images using hand-held cameras, the variation in  $t_z$  can be treated as negligible [15]. Hence, the motion can be described using only in-plane translations and rotation i.e.,  $t_x, t_y$  and  $\theta_z$  [15], [36]. These three dimensions constitute our 3D transformation space.

The transformation space can be sampled so as to obtain a finite set of transformations  $\mathbf{H}$  having  $N_{\mathbf{H}}$  different transformations. We assume that the bounds that we consider and the sampling rate of the transformation space contain the necessary transformations to approximately form the blurred image. The TSF  $h_T$  is a function that maps a transformation in  $\mathbf{H}$  to a non-negative real number i.e.,  $h_T : \mathbf{H} \rightarrow \mathbf{R}_+$ . For each transformation  $\Gamma \in \mathbf{H}$ , the value of the TSF  $h_T(\Gamma)$  denotes the fraction of the total exposure duration for which the camera was stationary in the position that caused the transformation. The final blurred intensity image in terms of the TSF can then be expressed as

$$Z = f \left( \sum_{k=1}^{N_{\mathbf{H}}} h_T(\Gamma_k) \Gamma_k(E) \Delta t \right) \quad (4)$$

This relation when discretized can be written as a linear equation as shown by Whyte *et. al* [34]. Thus, we can write  $Z = f(KE\Delta t)$ , where  $K$  is a large sparse matrix with the non-zero elements derived from TSF coefficients and bilinear weights. Note that (3) and (4) are different ways of expressing the same  $Z$ .

Note that each of the blurred observations in the HDR imaging problem is acted upon by a different TSF and these TSFs must be estimated in order to reveal camera motion. In [34] and [15], a blind estimation method is used for finding the TSF. We believe that such an approach is not suitable for finding multiple TSFs simultaneously since it does not utilize the information available in different observations. Our procedure to estimate the TSF is as follows. The local PSFs of a blurred image can be related to the TSF as

$$h(i, j; m, n) = \sum_{k=1}^{N_{\mathbf{H}}} h_T(\Gamma) \delta_d(m - (i_\Gamma - i), n - (j_\Gamma - j)) \quad (5)$$

where  $(i_\Gamma, j_\Gamma)$  denotes the position when transformation  $\Gamma^{-1}$  is applied on  $(i, j)$ ,  $h$  is the PSF at  $(i, j)$ , and  $\delta_d$  denotes

the 2D Kronecker delta function. Each local PSF can be considered as a weighted sum of the components of the TSF of the image. If  $N_p$  such PSFs are known, each PSF can be related to the TSF as  $h_{\mathbf{p}_l} = M_l h_T$  where  $l = 1 \dots N_p$ ,  $M_l$  is a matrix whose entries are determined by the location  $\mathbf{p}_l$  of the blur kernel and interpolation coefficients. Stacking all such relations leads to the linear relation  $\bar{h} = \mathbf{M}h_T$  where  $\mathbf{M}$  is a large sparse matrix. Camera shake results in motion that can be represented with only a small subset of transformations. Hence, we enforce a sparsity prior on the TSF. The cost function to derive the TSF which is consistent with the observed blur kernels is given by

$$\text{argmin } \|\bar{h} - \mathbf{M}h_T\|_2 + \lambda_s \|h_T\|_1 \quad (6)$$

The sparsity constraint is enforced by the  $l_1$ -norm term of equation (6). To minimize the cost function, we use the toolbox available at [19]. For accurate TSF estimation, we need the locations of the PSFs to be spread across the image so as to effectively capture the variations in blur due to camera motion. The procedure for PSF estimation which is critical for TSF computation will be discussed in the following section.

### III. IRRADIANCE ESTIMATION

In this section, we discuss irradiance estimation from a set of  $N_E$  differently exposed intensity images  $Z_1, Z_2 \dots Z_{N_E}$ . To each input image  $Z_i$ , we associate TSF  $K_i$ ,  $i = 1, 2, \dots, N_E$ . The irradiance image map  $B_i$  corresponding to observation  $Z_i$  is given by  $B_i = f^{-1}(Z_i)/\Delta t_i$ , where  $\Delta t_i$  is the exposure time of the observation  $Z_i$ . For a particular camera setting, we derive the camera response offline [6].

Simultaneous de-blurring and extraction of latent HDR irradiance image can be posed as an optimization problem where the solution can be obtained by minimizing the cost

$$\sum_{i=1}^{N_E} \|K_i E - B_i\|^2. \quad (7)$$

Here,  $E$  denotes latent irradiance image while  $K_i$  is the blurring matrix of the  $i^{\text{th}}$  exposure that represents the space-variant blurring operation. The rows of  $K_i$  are local blur filters acting on the pixels of  $E$  to yield the blurred irradiance image  $B_i$ . The summation in (7) can be removed by stacking all the blurred irradiance images ( $B_i$ s) into a single matrix  $\tilde{B}$  and the corresponding  $K_i$ s into a single matrix  $\tilde{K}$  so as to arrive at  $\|\tilde{K}E - \tilde{B}\|^2$ . Considering the effect of truncation due to the CRF, we introduce a mask in equation (8) which is derived based on the gray scale image equivalent of the observations  $Z_i$ . A pixel which is saturated in different exposures leads to different irradiance values, but patches with intensities neither too low nor too high lead to comparable irradiances. A mask was also applied in [5], [35] to restrict the influence of saturated pixels. However, even the lower intensities can get clipped. Consequently, we propose to use masks that are generated from a 256-point (corresponding to each intensity value) Tukey window which has a smooth transition at both ends when going from 0 to 1. The smoothness is controlled by a parameter  $\alpha$ . Figure 2(a) shows the Tukey window for

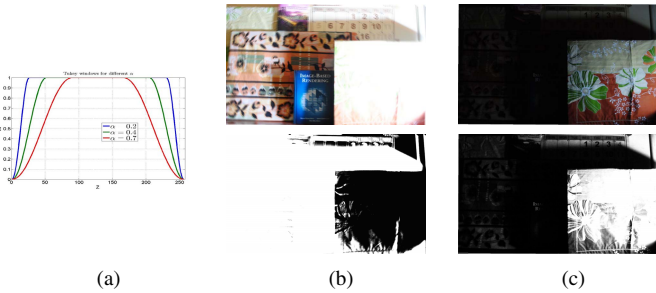


Fig. 2. (a) Plot of Tukey window for different values of  $\alpha$ . (b) and (c) Frames corresponding to different exposure times and their respective masks.

different values of  $\alpha$ . The masks obtained for images captured at exposure times  $\frac{1}{30}$ s and 1s are shown in Figures 2(b) and (c) for  $\alpha = 0.3$ . Note that the masks calculated from the Tukey window restrict the effect of both saturated and low-intensity pixels. The  $\alpha$  values must be selected based on the shape of the CRF and the intensity distribution of an image. The same mask is applied to all the color channels for maintaining color balance. Incorporating the effect of masks yields the new modified cost

$$\|\bar{m}\tilde{K}E - \bar{m}\tilde{B}\|^2 \quad (8)$$

where  $\bar{m}$  is a large diagonal matrix containing all the masks corresponding to different exposure times. Each input observation has a different mask depending on the intensity values of that image. The mask values are arranged along the diagonal.

It is a known fact that deblurring algorithms require imposition of priors to reduce deconvolution artifacts. We employ the total variation (TV) prior for regularization as it assists in suppressing image noise while simultaneously preserving the edges. The equivalent cost function after incorporating regularization is given by

$$O = \underset{E}{\operatorname{argmin}} \|\bar{m}\tilde{K}E - \bar{m}\tilde{B}\|^2 + \lambda_{TV} \int |\nabla E| \quad (9)$$

We solve the above equation iteratively using conjugate-gradient by employing the half-quadratic scheme [30]. The derivative of the cost function yields

$$\frac{\partial O}{\partial E} = \bar{m}\tilde{K}^T(\bar{m}(\tilde{K}E - \tilde{B})) - \lambda_{TV} \left( \nabla \frac{\nabla E}{|\nabla E|} \right) \quad (10)$$

where  $E$  is the irradiance image that changes in each iteration and  $K^T$  represents the adjoint of the blurring operation and corresponds to inverse warping [31]. The term  $\tilde{K}E$  is obtained by blurring  $E$  using TSFs that are present in  $K$ . Blurring is carried out by warping the irradiance image using the TSFs present in  $\tilde{K}$ .

In section II-B, we had discussed TSF estimation from locally determined PSFs (equation (6)). Interestingly, in the estimation of PSFs, two different scenarios arise depending on whether some or all the observations are blurred. We now discuss these two cases separately in more detail.

#### A. Non-Blurred/Blurred Observations

It is reasonable to assume that no blurring will occur for short exposure times since the displacement of the camera will

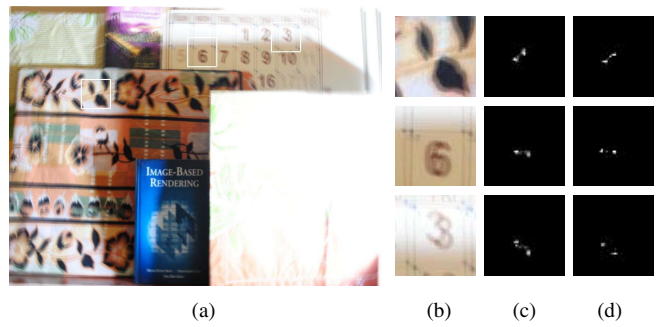


Fig. 3. (a) The selected patches are marked in the blurred image. (b) The selected patches, (c) the corresponding true PSF and (d) the estimated PSFs for each patch.

be negligible during that period. The TSFs of the non-blurred observations consist of a unit weight at the transformation corresponding to zero translation and rotation. Suppose the threshold limit for blurring is taken to be  $\tau_{bs}$ . Then, images captured beyond this exposure duration setting can be treated as blurred. The lower exposures provide unblurred scene irradiance only in certain regions. The higher exposures contain information that is not available in the lower exposures. However, this information cannot be utilized directly as it is blurred. The patches used for PSF estimation are manually selected such that the pixels contain intensities in the mid-range in order to avoid the clipping effect. While it should be possible to automatically select patches such that they reasonably sample different regions of the image (as discussed in section II-B), deciphering whether a patch is well-suited for blur kernel estimation remains an open problem.

In order to find the local PSFs of a blurred frame  $Z_s$ , local patches from  $Z_s$  and a non-blurred lower exposure (say)  $Z_r$  are cropped. If there are multiple non-blurred observations, then  $Z_r$  corresponds to the one with the highest exposure duration. Within a blurred frame, we consider  $N_p$  different image patches at image locations  $\mathbf{p}_1 \mathbf{p}_2 \dots \mathbf{p}_{N_p}$ . The blur is assumed to be locally space-invariant. For each blurred patch in  $Z_s$ , it is reasonable to assume that  $B_{\mathbf{p}_l}^s = E_{\mathbf{p}_l}^r * h_{\mathbf{p}_l}^s$  where  $B_{\mathbf{p}_l}^s$  is the irradiance patch in  $Z_s$  at location  $\mathbf{p}_l$ ,  $E_{\mathbf{p}_l}^r$  is the corresponding latent irradiance image patch obtained from  $Z_r$  (an unblurred frame),  $h_{\mathbf{p}_l}^s$  is the blur at location  $\mathbf{p}_l$  of the blurred frame  $Z_s$ , and  $*$  denotes convolution. We again apply a mask to limit any clipping effect caused by the CRF as done in equation (8) while estimating the latent scene irradiance. Here, masked patches of  $Z_s$  and  $Z_r$  corresponding to location  $\mathbf{p}_l$  are cropped and an equivalent mask  $m = m_{\mathbf{p}_l}^s \cdot m_{\mathbf{p}_l}^r$  is derived. Each of the blur kernels  $h_{\mathbf{p}_l}^s$  is then individually estimated by minimizing

$$\underset{h_{\mathbf{p}_l}^s}{\operatorname{argmin}} \left\| \left( m \cdot B_{\mathbf{p}_l}^s - m \cdot (h_{\mathbf{p}_l}^s * E_{\mathbf{p}_l}^r) \right) \right\|^2 \quad (11)$$

using conjugate-gradient. The local PSFs of all the blurred frames is estimated in the above manner. Note that the entire estimation scheme is carried out in the irradiance domain. Figure 3(a) shows a synthetically blurred image with boxes around select patches. The image patches and the true PSFs and estimated PSFs corresponding to these patches are shown in Figures 3(b) to (d).

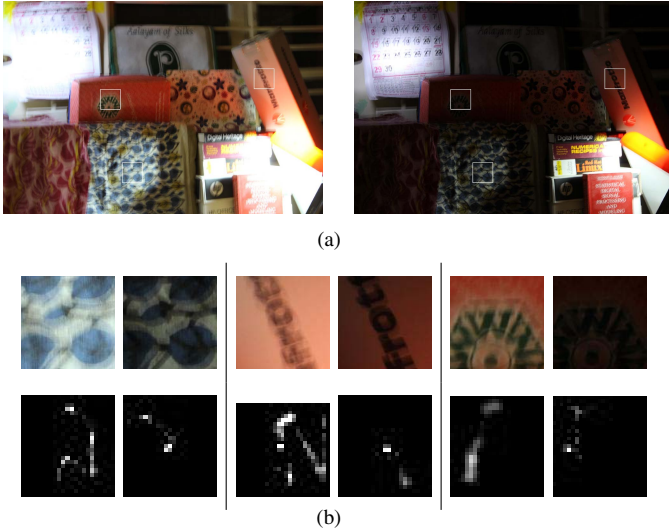


Fig. 4. PSF estimation for all-blurred observations. (a) Blurred data from which the local PSFs are estimated. (b) The first row shows three pairs of patches from two blurred observations, while the second row shows the corresponding estimated PSFs.

### B. All-Blurred Observations

If all the images in the dataset are blurred, then the PSF estimation discussed in section III-A is no longer valid. Such a situation arises when all the observations are captured using exposure times above  $\tau_b$  seconds. One could consider blind estimation techniques such as [10] (single channel) or [30] (multi-channel) to estimate the PSFs. In order to be able to exploit all the information available, we adopt the multi-channel approach. Following [30], we estimate  $N_p$  different PSFs of a blurred frame corresponding to local irradiance image patches  $B_{\mathbf{p}_j}^k$ , where  $\mathbf{p}_j$  refers to the location of the patch ( $j = 1, 2, \dots, N_p$ ), and  $k$  is the index of the frame. At a location  $\mathbf{p}_j$ , the PSFs of the two selected frames ( $n = 1, 2$ ) are derived by minimizing the following energy function

$$\Theta(E_{\mathbf{p}_j}, h_{\mathbf{p}_j}^1, h_{\mathbf{p}_j}^2) = \frac{1}{2} \sum_{n=1}^2 \|h_{\mathbf{p}_j}^n * E_{\mathbf{p}_j} - B_{\mathbf{p}_j}^n\|^2 + \lambda_{TV} \int |\nabla E_{\mathbf{p}_j}| + \frac{1}{2} \cdot \lambda_h \|h_{\mathbf{p}_j}^2 * B_{\mathbf{p}_j}^1 - h_{\mathbf{p}_j}^1 * B_{\mathbf{p}_j}^2\|^2 \quad (12)$$

where  $\lambda_{TV}$  and  $\lambda_h$  are regularization parameters,  $E_{\mathbf{p}_j}$  is the estimated latent scene irradiance patch at  $\mathbf{p}_j$ , the quantities  $h_{\mathbf{p}_j}^1$  and  $h_{\mathbf{p}_j}^2$  are the estimated PSFs at location  $\mathbf{p}_j$  corresponding to blurred irradiance patches  $B_{\mathbf{p}_j}^1$  and  $B_{\mathbf{p}_j}^2$  in the two selected observations. Following the above procedure,  $N_p$  different PSFs are estimated for each of the blurred frames. Figure 4 shows a pair of non-uniformly blurred images, the local patches ( $120 \times 120$ ) and the estimated PSFs ( $25 \times 25$ ).

The space-invariant PSFs thus estimated satisfy  $B_{\mathbf{p}_j}^n = h_{\mathbf{p}_j}^n * E_{\mathbf{p}_j}$ . However, note that even the relation  $B_{\mathbf{p}_j}^n = \mathbf{S}^{-1}(h_{\mathbf{p}_j}^n) * \mathbf{S}(E_{\mathbf{p}_j})$  where  $\mathbf{S}$  is a translational shift (along  $x$  and/or  $y$  directions) is also equally valid. Thus, the PSFs that we estimate using equation (12), though locally accurate, might not be in mutual alignment with respect to the PSFs estimated at other locations. If we attempt to use these PSFs directly in

the TSF estimation procedure discussed in section II, then the TSF thus estimated will be erroneous. The true TSFs cannot be estimated without compensating for the shifts among the underlying PSFs. To alleviate this problem, we (randomly) choose one of the PSFs as reference and align other PSFs with respect to it. If  $h_{\mathbf{p}_1}^1, h_{\mathbf{p}_2}^1 \dots h_{\mathbf{p}_{N_p}}^1$  are the PSFs of the first frame, we choose one of the PSFs (say  $h_{\mathbf{p}_{ref}}^1$ ) as reference. The TSF  $h_T^1$  is estimated by searching over all possible shifts of the PSFs  $h_{\mathbf{p}_1}^1$  to  $h_{\mathbf{p}_{N_p}}^1$ . For each possible shift,  $h_T^1$  is computed using equation (6) and that  $h_T^1$  which minimizes the error  $\sum_{l=1}^{N_p} \|h_{\mathbf{p}_l}^1 - M_l h_T^1\|^2$  is chosen to be the correct one. Note that as a shifted PSF can have correspondingly shifted latent image, many possible solutions for the TSF with correspondingly warped latent images can exist. Hence, the solution (TSF) obtained by our procedure will correspond to one of the warped instances.

The alignment process discussed above, however, does not ensure inter-frame alignment of TSFs. Let  $h_T^{ref}$  be the reference TSF obtained after aligning the blur kernels in one of the frames. Strictly speaking, the TSFs for other blurred frames cannot be calculated independently of  $h_T^{ref}$ . Suppose  $h_{\mathbf{p}_1}^2, h_{\mathbf{p}_2}^2 \dots h_{\mathbf{p}_{N_p}}^2$  are PSFs estimated for the second frame estimated using equation (12). Then, the PSFs  $h_{\mathbf{p}_1}^{ref}, h_{\mathbf{p}_2}^{ref} \dots h_{\mathbf{p}_{N_p}}^{ref}$  at the corresponding locations in the reference frame can be calculated as  $h_{\mathbf{p}_l}^{ref} = M_l h_T^{ref}$ . Therefore, an ideally compensated  $h_{\mathbf{p}_l}^2$  minimizes the error  $\|h_{\mathbf{p}_l}^2 * B_{\mathbf{p}_l}^{ref} - h_{\mathbf{p}_l}^{ref} * B_{\mathbf{p}_l}^2\|^2$  where  $B_{\mathbf{p}_l}^{ref}$  and  $B_{\mathbf{p}_l}^2$  are the blurred irradiance patches of the reference frame and second frame, respectively at location  $\mathbf{p}_l$ . The correct TSF  $h_T^2$  corresponding to the second frame is obtained from equation (6) using these compensated PSFs  $h_{\mathbf{p}_l}^2$ . The same procedure is followed for finding the TSFs of all the blurred frames. The issue of aligning TSFs did not arise in section III A since the reference image was a fixed and unblurred frame<sup>1</sup>.

## IV. EXPERIMENTAL RESULTS

We demonstrate the effectiveness of our method for both the scenarios discussed in section III with synthetic and real experiments. Fujifilm HS-10 and Canon 60D cameras were employed to capture the data for the experiments. The response functions of these cameras for pre-set parameters were calculated off-line [6]. To display the HDR irradiance estimated by our algorithm, we use the tone-mapping feature of Adobe Photoshop.

We initially tested our scheme for the case of non-blurred/blurred observations. We first captured unblurred images of a static scene for exposure times of  $\frac{1}{30}, \frac{1}{8}, \frac{1}{5}, \frac{1}{2}$  and 2s using a tripod and these are shown in Figure 5. Next, the observations corresponding to exposure times of  $\frac{1}{2}$ s and 2s were blurred using synthetically generated TSFs and these are shown in Figure 5. The TSFs were generated to represent general camera motion caused by camera-shake. The TSF dimensions  $t_x$  and  $t_y$  took integer values in the range

<sup>1</sup>In supplementary material, we demonstrate the accuracy of determining TSF from PSFs using synthetic examples.

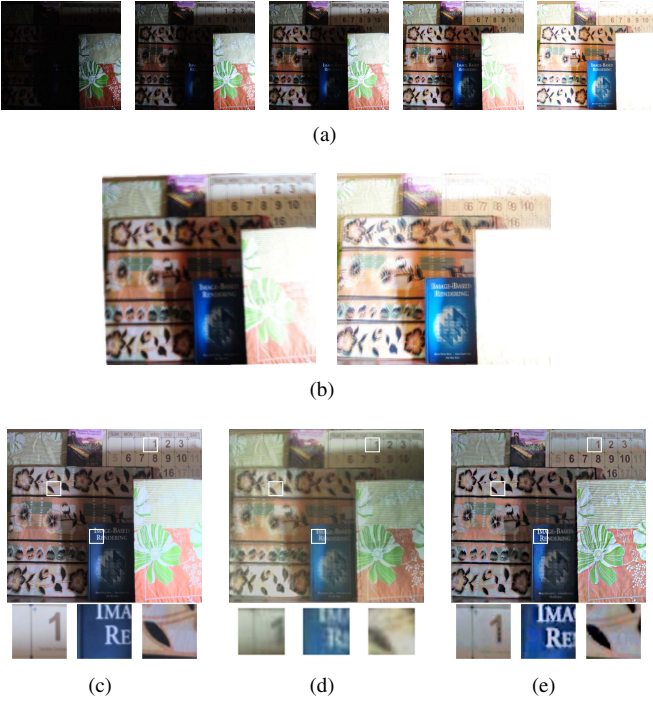


Fig. 5. Synthetic experiment for the case of blurred higher exposures. (a) Image set captured with exposure times of  $\frac{1}{30}$ ,  $\frac{1}{8}$ ,  $\frac{1}{5}$ ,  $\frac{1}{2}$  and 2s. (b) Synthetically blurred higher exposures for  $\frac{1}{2}$ s and 2s. HDR image and its zoomed-in patches obtained from (c) non-blurred, registered image set, (d) deblurred images using [34], and (e) our method.

$[-12, 12]$  in steps of 1 pixel. Rotation  $\theta_z$  ranged between  $-1.5$  and  $1.5$  degrees in steps of  $0.25$  degrees.

Using the approach described in section III-A, the local PSFs of these two blurred images were estimated using the non-blurred input image corresponding to exposure time of  $\frac{1}{5}$ s. The corresponding TSFs were found following the steps explained in section II. Finally, the latent scene irradiance was estimated by minimizing the cost given in section III. The tone-mapped low dynamic range result was obtained as shown in Figure 5. The HDR image obtained from the non-blurred dataset using [6] is shown in Figure 5. We treat this to be the optimal HDR solution and use it to evaluate the performance of our method. It can be seen that our result is quite well-composed. Akin to the image in Figure 5 the details in the scene are clearer in our output. The front illuminated part is clearly visible without any saturation. Even darker regions such as the book title and the booklet at the top have become discernible. The visibility of the numbers on the chart improves with exposure time and these are uniformly lit in our result. We also compared our result with that of a naive approach. The higher exposures were subject to blind deblurring [34] and the irradiance was estimated from the deblurred observation using [6] to obtain the result shown in Figure 5(d). From the zoomed-in patches of Figure 5(d), we observe that the result of a naive approach contains residual blur. In our framework, we judiciously exploit the tight coupling that inherently exists between the latent scene irradiance and each of the differently exposed and blurred observations. Since our deblurring step subsumes all the blurred observations, our result is superior.

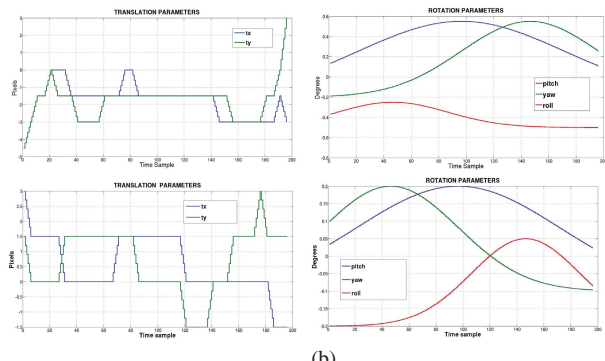
We next considered the scenario in which the dataset consisted of only blurred observations. The unblurred images of the static scene considered in the earlier experiment and corresponding to exposure times  $\frac{1}{30}$ ,  $\frac{1}{8}$  and 1s were blurred using different synthetically generated TSFs. The blurred LDR images are shown in Figure 6(a). The local PSFs for each of the images were estimated using the method discussed in section III-B. The implementation of this PSF estimation process was built upon the code provided by Sroubek and Flusser [30]. The intra and inter-frame alignment of the estimated PSFs were then carried out as described in section III-B. The TSFs of all the blurred images were recovered using these aligned PSFs. From the three blurred observations, the latent scene irradiance was finally estimated by minimizing equation (9). The resultant tone-mapped HDR image is shown in Figure 6(b). The effectiveness of our method is clearly visible from the uniform illumination of the scene and is also highlighted by the close-ups shown in Figure 6(c). The numbers on the chart in our result appear sharp and correctly illuminated although they were either blurred or invisible in the input images. The vines and leaves pattern appear sharp and uniformly lit and so does the flower pattern shown in the next patch. For the purpose of comparison, we also applied the algorithm of [21] on our data and the output is shown in Figure 6(d). From the result we observe that while certain portions of the image such as the front illuminated part shown in the first patch in Figure 6(e) are deblurred, the output is hazy in areas such as the numerals on the chart shown in the second patch. The limitation of the uniform blur model of [21] is highlighted by the residual blur present in the image as indicated in the third patch of Figure 6(e).

When the scene is approximately of a constant depth, blurring due to general camera motion can be modeled using only a 3D TSF (in terms of  $t_x$ ,  $t_y$  and  $\theta_z$ ) as demonstrated in [15] for single image deblurring in the intensity domain. We investigated the validity of this assumption in the irradiance domain using a synthetic example. The images including the blurred higher exposures are shown in Figure 7(a). The higher exposures were blurred considering general camera motion including out-of-plane rotations. The parameters of camera pose at each instant of time during exposure are shown in Figure 7(b). The camera motion was selected so as to depict a realistic camera-shake where the effect of  $t_z$  is insignificant. Even though the images were blurred with higher dimensional TSFs, we applied our method (section II and III) to estimate the blur using only 3D TSFs. The deblurred HDR irradiance image that we arrived at is shown in figure 7(c). The result is sharp and the improvement in visibility of the scene is also clearly discernible.

The data for real experiments was captured unconstrained with a hand-held camera. The first case where only the higher exposures are blurred was obtained in an outdoor scene. The images corresponding to different exposures are shown in Figure 8(a). These were captured for exposure times of  $\frac{1}{100}$ s,  $\frac{1}{50}$ s and  $\frac{1}{2}$ s by manually changing the shutter speeds. Only the highest exposure of  $\frac{1}{2}$ s was found to be blurred. The deblurred HDR result obtained after applying our method on this dataset is shown in Figure 8(b). The result establishes



Fig. 6. Synthetic experiment for HDR imaging with all-blurred images. (a) Synthetically blurred dataset. (b) Tone-mapped HDR result. (c) The first three rows are close-up patches of blurred input data at different locations. The fourth row consists of our output result at those locations. (d) Result obtained using [21] (e) Zoomed-in patches taken from (d).

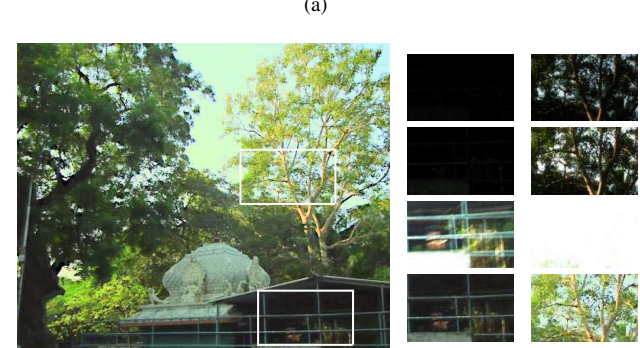


(a) Synthetic data set blurred by free camera motion.



Fig. 7. Verification of 3D-TSF assumption for 6D camera motion. (b) The translation (column 1) and rotational (column 2) parameters of the two TSFs. (c) Deblurred HDR result.

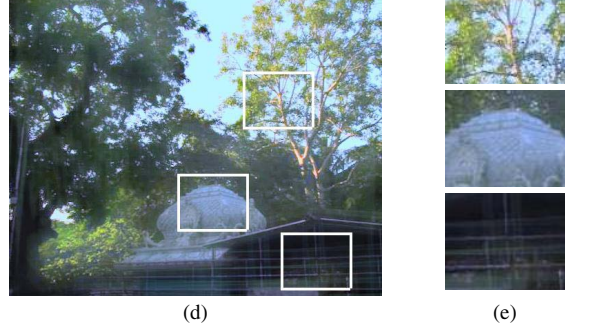
the claim of achieving the twin objectives of HDR imaging and deblurring. The close-ups shown in the two columns of Figure 8(c) highlight the effectiveness of our algorithm. The railings are visible only in the highest exposure of  $\frac{1}{2}$ s but are blurred. However, the railings are deblurred in our final result. The darker background region behind the railing is also visible in the result. In the second close-up which is of an illuminated region, the data is available only in the lower non-blurred exposures but is completely saturated in the higher exposure. The output obtained by applying the convolution model of [21]



(b)



(c)



(d)



(e)

Fig. 8. Real HDR imaging experiment with blurred higher exposures captured using a hand-held camera. (a) Real dataset captured with exposure times  $\frac{1}{100}$ ,  $\frac{1}{50}$  and  $\frac{1}{2}$ s. (b) The final deblurred HDR result. (c) Close-up patches from the input observations are shown in the first three rows while the corresponding output patch from our method is shown in the last row. (d) Result obtained using [21] which restricts the blur model to in-plane translations only. (e) Zoomed-in patches from (d).

is shown in Figure 8(d). This result is correctly lit in all regions. The image is sharp in the center and regions obtained from lower exposures as indicated by the top two patches of Figure 8(e). However, the lower patch shows remnant blur near the railings which is due to camera rotation. This result again underlines the need for using the space-variant blur model.

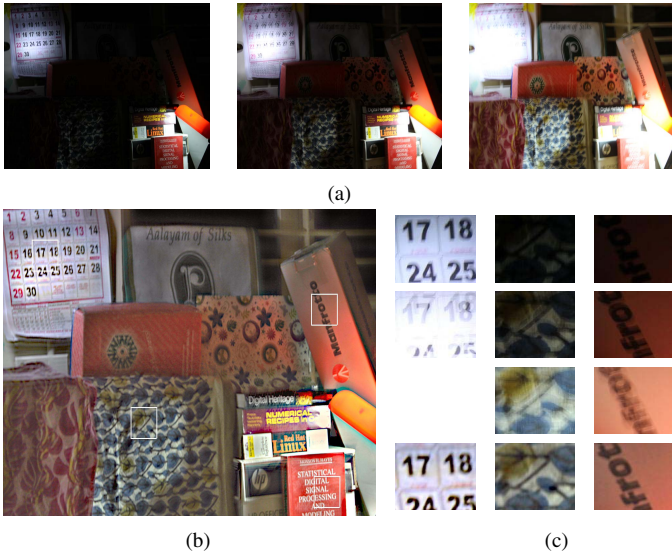


Fig. 9. Real HDR imaging experiment with differently exposed, non-uniformly blurred images. (a) Real dataset containing images captured with exposure durations of  $\frac{1}{6}$ ,  $\frac{1}{2}$  and 2s, respectively. (b) Final HDR result. (c) The zoomed-in patches of the input observations are placed in the first three rows and the corresponding output using our method is in the final row.

In the next experiment, we consider a scenario wherein all the observations are blurred. Figure 9(a) shows images captured at  $\frac{1}{6}$ ,  $\frac{1}{2}$  and 2s. In the second frame, note that the numbers on the calendar are highly blurred compared to “manfrotto” on the right-hand-side of the frame. The final output shown in Figure 9(b) is clearly a collection of the best possible information at each pixel. A few cropped close-up patches are highlighted in the fourth row of Figure 9(c). The calendar region which is saturated in the highest exposure and severely blurred in the mid-exposure and hazy in the lower exposure is vivid in the final result. For the second patch, the image is hardly visible in the lowest exposure but is highly blurred in the other two exposures. The final output is deblurred and well-lit. The third patch has minimal blur in the mid exposure, but appears degraded in other frames. Our scheme restores it too with uniform illumination.

In the following experiment, a sun-lit window scene was considered as shown in Figure 10(a). The geometric shifts among the frames was large in this example. The images were captured with exposure durations of  $\frac{1}{40}$ ,  $\frac{1}{15}$ ,  $\frac{1}{4}$  and 1s. The window pane at the top portion of the image is saturated in all the exposures except in the lowest exposure. The rest of the scene reveals a wide range of illumination differences. In Figure 10(d), we show some of the patches from the three highest exposures in the first three columns. These were cropped from the same locations in all the frames. Note that they not only have different amounts of illumination and blurring but also show significant mutual shifts. Although these shifts can possibly be compensated by the estimated PSFs, the kernels will have to be very big which can further complicate the already ill-posed problem. Thus, it is beneficial to register the different exposures before proceeding with the steps described in section III. We perform SIFT-based registration [20] to identify affine transformations between frames despite illumination differences in the exposed images.

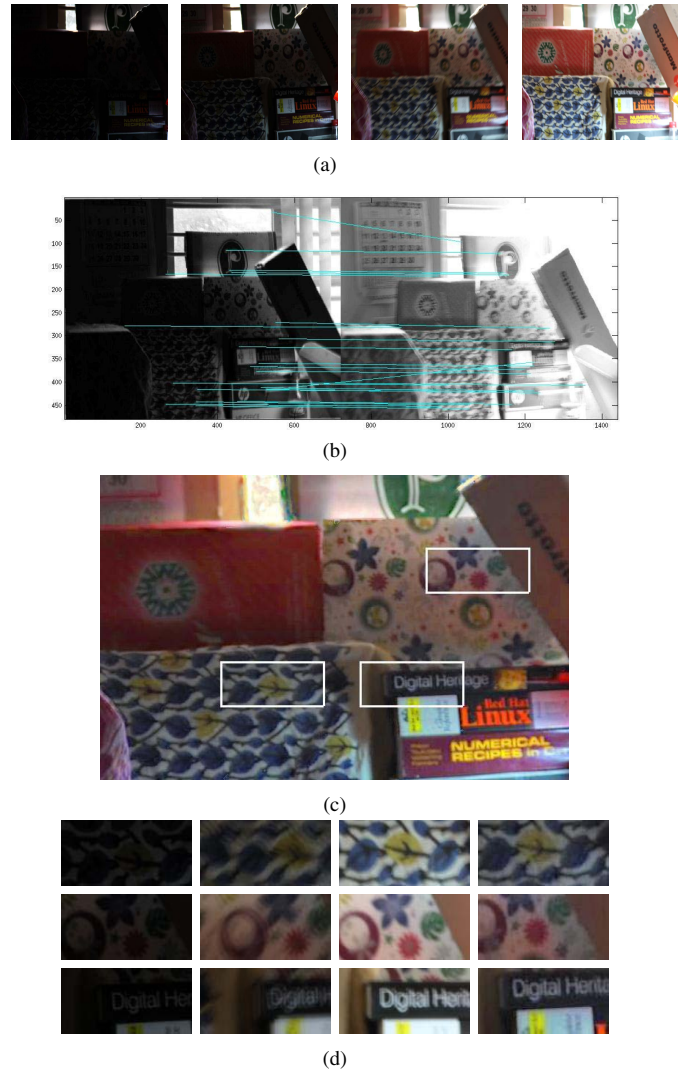


Fig. 10. Real HDR imaging experiment in a highly illuminated scenario. (a) Dataset captured from a hand-held camera for exposure times  $\frac{1}{40}$ ,  $\frac{1}{15}$ ,  $\frac{1}{4}$  and 1s. The lower exposures of  $\frac{1}{40}$ s and  $\frac{1}{15}$ s are relatively less blurred than the higher exposures. (b) Matching SIFT features between two blurred images captured with different exposure settings. (c) The final HDR result. (d) Close-up patches of the different input observations ( $\frac{1}{15}$ ,  $\frac{1}{4}$  and 1s) are shown in the first three columns and the corresponding result is shown in the last column.

Since we assume the scene to be flat, compensating for affine movement is sufficient to register the frames. In our experiment, the number of matching points for non-blurred exposures was more than 100. However, when blurred higher exposures are registered with respect to a non-blurred lower exposure, it was observed that the number of feature points decrease. When both the exposures are blurred, this reduces to about 25 matching points (Figure 10(b)). However, this is still much higher than the minimum requirement of 4 points for affine warping. The final output of our scheme after registering the frames is shown in Figure 10(c). Note that our result is uniformly illuminated almost throughout the scene. Note that the first cropped patch exhibits sharp boundaries. The orb and star pattern in the second patch appear sharp in the output although they are blurred in the input observations. The clarity of the word “DIGITAL” in the third patch shows

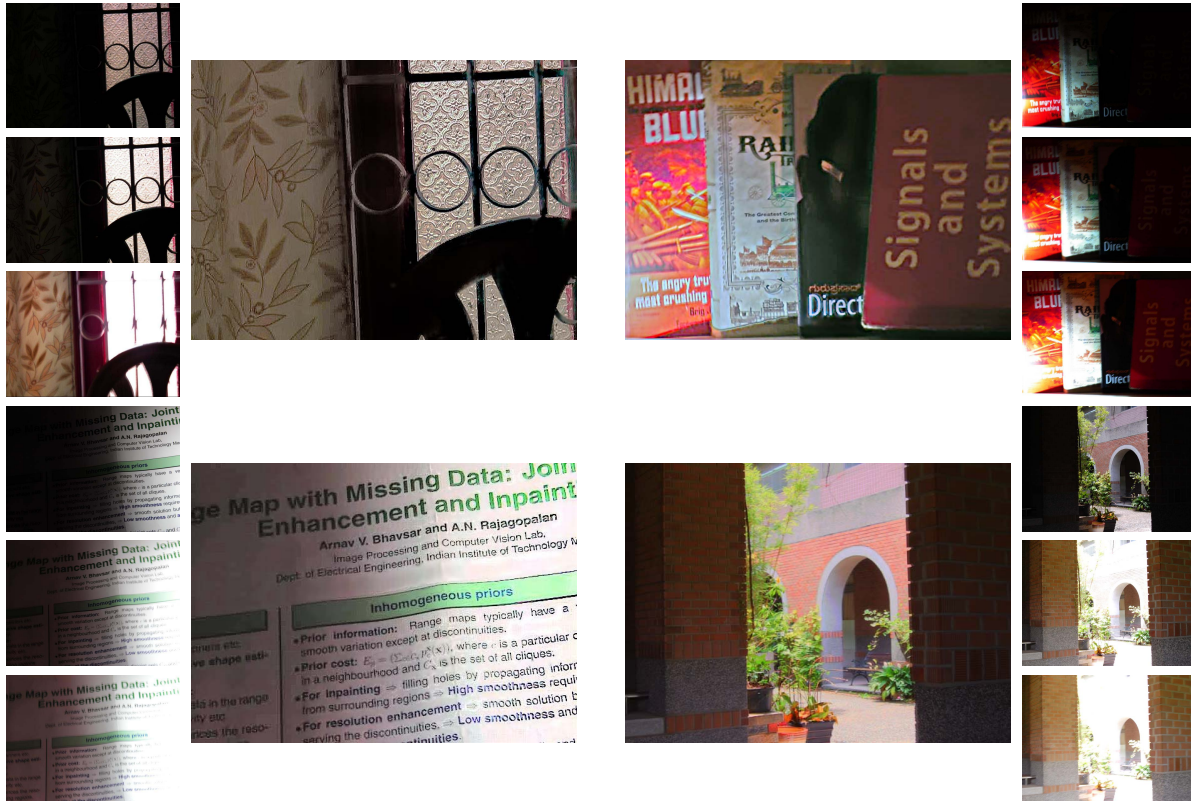


Fig. 11. First and fourth columns: blurred and differently exposed observations. Second and third columns: results from the proposed method.

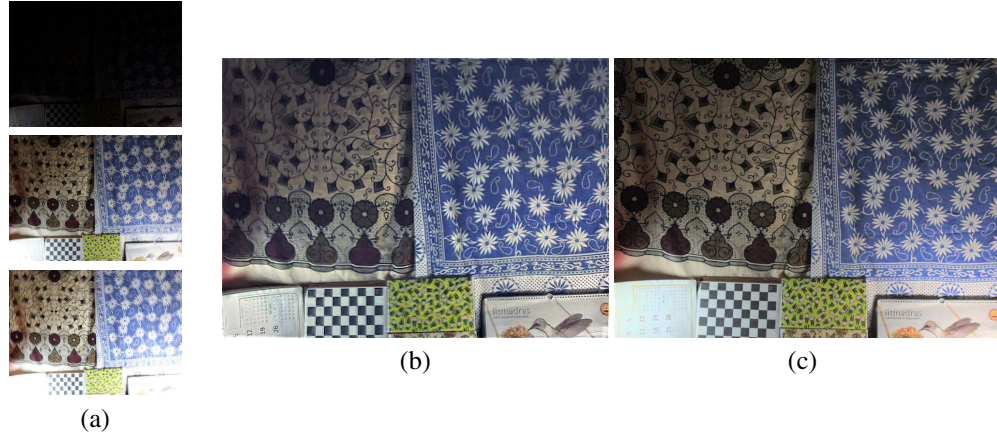


Fig. 12. (a) Observations. (b) Result of the proposed method from the observations in (a). (c) Result obtained from observations captured with a still camera.

the deblurring capability of our method along with the ability to render uniform illumination.

We next tested the performance of our method on a few more scenes (Figure 11) consisting of a sunlit window beside a dark wall, a set of books, a poster, and an arch from the dataset of [21]. In Figure 11, the observations are shown in the first and fourth columns, while the corresponding results of our method are shown in the second and third columns respectively. We notice that in each of these examples, the resultant LDR representation is well-composed as well as deblurred.

In our next experiment, we compare the result of our method against an ideal scenario wherein images were captured by

placing the camera on a tripod. Using the blurred observations shown in Figure 12 (a), the result from the proposed method is as shown in Figure 12 (b). By applying the standard technique in [6] on the blur-free images, the irradiance image was obtained as shown in Figure 12 (c). Note that our result closely matches the result obtained from the ideal scenario.

To also quantify the performance of our method, we evaluated the results of our method using a recently proposed measure that can assess the quality of an image based on the extent of blurring [12]. For the sake of comparison, in each of our experiments, we directly estimated the LDR representation using the exposure fusion technique of [23] (without accounting for blur) and evaluated the quality of the

resultant image. The average improvement in quality score due to our approach was found to be approximately double on our dataset.

## V. CONCLUSION

In this paper, we discussed a method for estimating the latent high dynamic range irradiance of a scene in the presence of non-uniform motion blur due to camera-shake. We proposed a two-step approach for achieving the dual objectives of deblurring and HDR imaging. First, the sparse TSFs of all the blurred images are estimated using their local PSFs. The scene irradiance was then estimated by minimizing a suitably derived cost involving all the frames. The issue of alignment of the estimated PSFs was also discussed as this is critical for the success of the overall process.

There are different possible directions to pursue to further extend the scope of this work. When the scene is close to the camera, the effects of parallax cannot be ignored and the TSF space needs to be of a higher dimension. When there is a large registration error, we account for it using SIFT features. However, this may fail when the extent of blur is very severe or if the scene does not have enough distinguishable features. In such cases, region based registration techniques such as maximally stable extremal region (MSER) techniques in conjunction with SIFT descriptors [11] can possibly be tried. Finally, handling dynamic scenes in the presence of motion blur is a challenge in its own right.

## ACKNOWLEDGMENT

The authors wish to thank the anonymous reviewers for their useful comments and suggestions. They would also like to thank Filip Sroubek and Paul Debevec for sharing their codes.

## REFERENCES

- [1] (2013). *When Tripods are not Permitted* [Online]. Available: <http://www.shutterbug.com/content/when-tripods-are-not-permitted>
- [2] S. Bae, S. Paris, and F. Durand, “Two-scale tone management for photographic look,” *ACM Trans. Graph.*, vol. 25, no. 3, pp. 637–645, 2006.
- [3] J. Cai, H. Ji, C. Liu, and Z. Shen, “Framelet based blind motion deblurring from a single image,” *IEEE Trans. Image Process.*, vol. 21, no. 2, pp. 562–572, Feb. 2012.
- [4] P. Chandramouli and A. N. Rajagopalan, “Inferring image transformation and structure from motion-blurred images,” in *Proc. Brit. Mach. Vis. Conf.*, 2010, pp. 1–12.
- [5] S. Cho, J. Wang, and S. Lee, “Handling outliers in non-blind image deconvolution,” in *Proc. ICCV*, 2011, pp. 495–502.
- [6] P. E. Debevec and J. Malik, “Recovering high dynamic range radiance maps from photographs,” in *Proc. ACM SIGGRAPH*, 1997, pp. 369–378.
- [7] D. Doeffinger, *Creative Shutter Speed: Master Your Cameras Most Powerful Control*. New York, NY, USA: Wiley, 2009.
- [8] F. Durand and J. Dorsey, “Fast bilateral filtering for the display of high-dynamic-range images,” *ACM Trans. Graph.*, vol. 21, no. 3, pp. 257–266, 2002.
- [9] R. Fattal, D. Lischinski, and M. Werman, “Gradient domain high dynamic range compression,” *ACM Trans. Graph.*, vol. 21, no. 3, pp. 249–256, 2002.
- [10] R. Fergus, B. Singh, A. Hertzmann, S. T. Roweis, and W. T. Freeman, “Removing camera shake from a single photograph,” *ACM Trans. Graph.*, vol. 25, no. 3, pp. 787–794, 2006.
- [11] P. E. Forssen and D. G. Lowe, “Shape descriptors for maximally stable extremal regions,” in *Proc. IEEE 11th ICCV*, Oct. 2007, pp. 1–8.
- [12] S. Gabarda and G. Cristobal, “Blind image quality assessment through anisotropy,” *J. Opt. Soc. Amer. A, Opt. Image Sci. Vis.*, vol. 24, no. 12, pp. B42–B51, 2007.
- [13] M. D. Grossberg and S. K. Nayar, “Determining the camera response from images: What is knowable,” *IEEE Trans. Pattern Anal. Mach. Intell.*, vol. 25, no. 11, pp. 1455–1467, Nov. 2003.
- [14] M. D. Grossberg and S. K. Nayar, “Modeling the space of camera response functions,” *IEEE Trans. Pattern Anal. Mach. Intell.*, vol. 26, no. 10, pp. 1272–1282, Oct. 2004.
- [15] A. Gupta, N. Joshi, C. Lawrence Zitnick, M. Cohen, and B. Curless, “Single image deblurring using motion density functions,” in *Proc. ECCV*, 2010, pp. 171–184.
- [16] S. W. Hasinoff and K. N. Kutulakos, “Multiple-aperture photography for high dynamic range and post-capture refocusing,” *IEEE Trans. Pattern Anal. Mach. Intell.*, vol. 1, no. 1, pp. 1–17, Jan. 2009.
- [17] S. Kim, Y. W. Tai, S. J. Kim, M. S. Brown, and Y. Matsushita, “Nonlinear camera response functions and image deblurring,” in *Proc. CVPR*, 2012, pp. 25–32.
- [18] A. Levin, Y. Weiss, F. Durand, and W. Freeman, “Understanding blind deconvolution algorithms,” *IEEE Trans. Pattern Anal. Mach. Intell.*, vol. 33, no. 12, pp. 2354–2367, Nov. 2011.
- [19] J. Liu, S. Ji, and J. Ye, (2009). *SLEP: Sparse Learning with Efficient Projections*, Arizona State Univ., Phoenix, AZ, USA, [Online]. Available: <http://www.public.asu.edu/jye02/Software/SLEP>
- [20] D. G. Lowe, “Distinctive image features from scale-invariant keypoints,” *Int. J. Comput. Vis.*, vol. 60, no. 2, pp. 91–110, 2004.
- [21] P. Y. Lu, T. H. Huang, M. S. Wu, Y. T. Cheng, and Y. Y. Chuang, “High dynamic range image reconstruction from hand-held cameras,” in *Proc. CVPR*, 2009, pp. 509–516.
- [22] S. Mann, R. W. Picard, “Being ‘undigital’ with digital cameras: Extending dynamic range by combining differently exposed pictures,” in *Proc. 46th Annu. Conf. IS&T, Soc. Imag. Sci. Technol.*, 1995, pp. 422–428.
- [23] T. Mertens, J. Kautz, and F. Van Reeth, “Exposure fusion,” in *Proc. Pacific Conf. Comput. Graph. Appl.*, 2007, pp. 382–390.
- [24] T. Mitsunaga and S. K. Nayar, “Radiometric self calibration,” in *Proc. CVPR*, 1999, pp. 1–7.
- [25] S. Raman and S. Chaudhuri, “Bilateral filter based compositing for variable exposure photography,” in *Proc. Eurographics*, 2009, pp. 1–4.
- [26] R. Raskar, A. Ilie, and J. Yu, “Image fusion for context enhancement and video surrealism,” in *Proc. 3rd Int. Symp. Non-Photorealistic Animation Rendering Courses*, 2005, pp. 85–152.
- [27] E. Reinhard, M. Stark, P. Shirley, and J. Ferwerda, “Photographic tone reproduction for digital images,” *ACM Trans. Graph.*, vol. 21, no. 3, pp. 267–276, 2002.
- [28] Q. Shan, J. Jia, and A. Agarwala, “High-quality motion deblurring from a single image,” *ACM Trans. Graph.*, vol. 27, no. 3, pp. 1–73, 2008.
- [29] M. Sorel and J. Flusser, “Space-variant restoration of images degraded by camera motion blur,” *IEEE Trans. Image Process.*, vol. 17, no. 2, pp. 105–116, Feb. 2008.
- [30] F. Sroubek and J. Flusser, “Multichannel blind iterative image restoration,” *IEEE Trans. Image Process.*, vol. 12, no. 9, pp. 1094–1106, Sep. 2003.
- [31] Y. Tai, P. Tan, and M. S. Brown, “Richardson-Lucy deblurring for scenes under projective motion path,” *IEEE Trans. Pattern Anal. Mach. Intell.*, vol. 33, no. 8, pp. 1603–1618, Aug. 2011.
- [32] C. S. Vijay, P. Chandramouli, and A. N. Rajagopalan, “HDR imaging under non-uniform blurring,” in *Proc. ECCV Workshop Color Photometry Comput. Vis.*, 2012, pp. 451–460.
- [33] G. Ward, “Fast, robust image registration for compositing high dynamic range photographs from hand-held exposures,” *J. Graph. Tools*, vol. 8, no. 2, pp. 17–30, 2003.
- [34] O. Whyte, J. Sivic, A. Zisserman, and J. Ponce, “Non-uniform deblurring for shaken images,” in *Proc. CVPR*, 2010, pp. 491–498.
- [35] O. Whyte, J. Sivic, and A. Zisserman, “Deblurring shaken and partially saturated images,” in *Proc. IEEE Workshop CPCV, ICCV*, Nov. 2011, pp. 745–752.
- [36] O. Whyte, J. Sivic, A. Zisserman, and J. Ponce, “Non-uniform deblurring for Shaken images,” *Int. J. Comput. Vis.*, vol. 98, no. 2, pp. 168–186, 2012.

- [37] L. Yuan, J. Sun, L. Quan, and H. Shum, "Image deblurring with blurred/noisy image pairs," *ACM Trans. Graph.*, vol. 26, no. 3, pp. 1–11, 2007.
- [38] L. Zhang, A. Deshpande, and X. Chen, "Denoising vs. deblurring: HDR imaging techniques using moving cameras," in *Proc. CVPR*, Jun. 2010, pp. 522–529.



**Channarayapatna Shivaram Vijay** received the B.E. degree in telecommunication engineering from the M. S. Ramaiah Institute of Technology, Bangalore, India, in 2009, and the M.S. degree in electrical engineering from the Indian Institute of Technology, Madras, India, in 2012. He is currently a Research Consultant with Hewlett-Packard, India. His current research interests include computer vision, computational photography, and machine learning.



**Chandramouli Paramanand** received the B.E. degree in telecommunication engineering from the R. V. College of Engineering, Bengaluru, India, in 2004, and the M.S. degree in electrical engineering from the Indian Institute of Technology, Madras, India, in 2007, where he is currently pursuing the Ph.D. degree. His current research interests include computer vision and signal processing. He has worked on shape from optical and motion blur, image restoration, and high dynamic range imaging.



**Ambasamudram Narayanan Rajagopalan** received the Ph.D. degree in electrical engineering from the Indian Institute of Technology, Bombay, India, in 1998. In 1998, he was a Visiting Scientist with the Image Communication Laboratory, University of Erlangen, Erlangen, Germany. In 1998 and 2000, he was with the Center for Automation Research, University of Maryland, College Park, MD, USA, as an Assistant Research Scientist. He joined the Indian Institute of Technology, Madras, India, in October 2000, and is currently a Professor with the Department of Electrical Engineering. His current research interests include 3-D shape from optical and motion blur, image restoration, super-resolution, gait and face, and video matting. He is the co-author of *Depth from Defocus: A Real Aperture Imaging Approach* (Springer). He has held visiting positions with the Center for Automation Research, University of Maryland, in 2002 and 2005, and 2007 to 2008 as a Humboldt Fellow with the Technical University of Munich, Munich, Germany. He is a fellow of the Indian National Academy of Engineering. He served as an Associate Editor of the IEEE TRANSACTIONS ON PATTERN ANALYSIS AND MACHINE INTELLIGENCE from 2007 to 2011 and is currently an Associate Editor for IEEE TRANSACTIONS ON IMAGE PROCESSING. He was a Program Co-Chair for the seventh Indian Conference on Computer Vision, Graphics, and Image Processing in 2010 and was an Area Chair for the IEEE Conference on Computer Vision and Pattern Recognition in 2012. He is a recipient of the Outstanding Investigator Award from the Department of Atomic Energy, India, in 2012.



**Rama Chellappa** (F'92) received the B.E. (Hons.) degree in electronics and communication engineering from the University of Madras, Madras, India, in 1975, and the M.E. (with Distinction) degree from the Indian Institute of Science, Bangalore, India, in 1977. He received the M.S.E.E. and Ph.D. degrees in electrical engineering from Purdue University, West Lafayette, IN, USA, in 1978 and 1981, respectively. From 1981 to 1991, he was a Faculty Member with the Department of EE-Systems, University of Southern California (USC), Los Angeles, CA, USA. Since 1991, he has been a Professor of Electrical and Computer Engineering and a Professor of computer science with the University of Maryland (UMD), College Park, MD, USA. He is a Permanent Member with the Center for Automation Research, Institute for Advanced Computer Studies and he is serving as the Chair of the ECE Department. In 2005, he was a Minta Martin Professor of Engineering. His current research interests include face recognition, clustering and video summarization, 3-D modeling from video, image and video-based recognition of objects, events and activities, dictionary-based inference, compressive sensing, domain adaptation, and hyper spectral processing.

He received the NSF Presidential Young Investigator Award, four IBM Faculty Development Awards, the Excellence in Teaching Award from the School of Engineering at USC, and two paper awards from the International Association of Pattern Recognition (IAPR). He is a recipient of the K. S. Fu Prize from IAPR. He received the Society, Technical Achievement, and Meritorious Service Awards from the IEEE Signal Processing Society. He received the Technical Achievement and Meritorious Service Awards from the IEEE Computer Society. At UMD, he was elected as a Distinguished Faculty Research Fellow, as a Distinguished Scholar-Teacher, received an Outstanding Innovator Award from the Office of Technology Commercialization, and an Outstanding GEMSTONE Mentor Award from the Honors College. He received the Outstanding Faculty Research Award and the Poole and Kent Teaching Award for Senior Faculty from the College of Engineering. In 2010, he was recognized as an Outstanding ECE by Purdue University. He is a fellow of IAPR, OSA, and AAAS. He holds four patents.

Prof. Chellappa served as the Editor-in-Chief of the IEEE TRANSACTIONS ON PATTERN ANALYSIS AND MACHINE INTELLIGENCE. He has served as a General and Technical Program Chair for several IEEE international and national conferences and workshops. He is a Golden Core Member of the IEEE Computer Society and served as a Distinguished Lecturer of the IEEE Signal Processing Society. He completed a two-year term as the President of the IEEE Biometrics Council.